LHC Project Note 274

2001-12-18

Ian.Collins@cern.ch

Dynamic Gas Density in the LHC Interaction Regions 1&5 and 2&8 For Optics Version 6.3

I.R. Collins and O.B. Malyshev / LHC-VAC

Keywords: dynamic gas density, synchrotron radiation, photon, ion, electron stimulated desorption, conditioning

Summary

The dynamic gas densities in the Dispersion Suppressors (DS) and the Long Straight Sections (LSS) of Interaction Regions (IR), IR1&5 and IR2&8, excluding the experimental beampipes ±20m from the IP, estimated for optics version 6.3 in the first years of operation, are presented in this Note. Ion, photon and electron stimulated desorption determine the dynamic gas density in the LHC. Each mechanism is discussed in detail and combined to give, for the first time, a global picture of the dynamic gas density in these LSS. Assuming adequate installed pumping to ensure vacuum stability in both cryogenic elements (actively cooled beam screens with distributed pumping slots) and room temperature regions (lumped pumping), ion stimulated desorption may be neglected. In order to estimate the contribution from photon stimulated desorption, the sources of synchrotron radiation in the DS and the LSS in IR1&5 and IR2&8 are identified and quantified. Since photon and electron stimulated desorption yields change with dose, known as conditioning, certain assumptions are made regarding an operation scenario for the machine in the first years.

It is estimated that initially some room temperature regions of the machine may exhibit elevated gas densities, however, they will condition quickly to acceptable levels (defined here somewhat arbitrarily by the LHC lifetime limit), over the course of the 70 day running period. In the second year of operation the beam current is assumed to increase to 30% of the nominal with a corresponding increase in photon flux. At and above this current, beam induced electron multipacting is expected to become significant. Assuming a controllable heat load on the arc beam screen from the electron cloud at the level of 200mW/m, electron stimulated desorption is anticipated, resulting in an increased gas density. Due to the efficient conditioning of the vacuum chambers with electrons, the gas densities will recover quickly to acceptable levels; the higher the acceptable heat load in the cryogenic elements the more rapid the conditioning will be. Since the conditions for beam induced multipacting depend on many parameters such a chamber dimension, presence of magnetic field *etc*., conditioning is not expected to occur simultaneously around the machine. Dedicated commissioning fills may therefore be required to condition the vacuum chambers before physics runs. Once the nominal machine parameters are reached the vacuum system is expected to be fully conditioned and performing to specification.

1 Introduction

An Interaction Region (IR) of the LHC consists of a Long Straight Section (LSS) and the two adjacent Dispersion Suppressors (DS). The LSS is defined as the region between Q7 and Q7 encompassing an Interaction Point (IP). The DS is located between Q11 to the bending magnet before Q7 [1]. There are eight LSS, four containing high energy physics experiments: ATLAS at IP1, ALICE at IP2, CMS/TOTEM at IP5 and LHCb at IP8. The optics layouts of LSS1 and LSS5 are identical and symmetric about their IP. The optics layouts of LSS2 and LSS8 are not symmetric about their IP due to beam 1 injection in IR2 lhs and beam 2 injection in IR8 rhs.

The first estimation of the gas density, made in 1996, in the room temperature regions of the LHC assumed purely thermal out-gassing in a lumped pumped vacuum chamber [2]. More recent estimations were made for the regions between Q7 and D2 in IR1&5 for optics version 6.0, including photon stimulated desorption [3]. In this present note a more complete study, with all known beam induced effects, i.e. the dynamic beam vacuum during the first years of LHC operation, has been made for IR1&5 and IR2&8 using optics version 6.3. We focus our attention on the experimental IRs, excluding the experimental beampipes, i.e. $\pm$20 m from the IP (discussed elsewhere), thereby providing preliminary input for the optimisation of the vacuum system layout in the LSS. In addition this study provides valuable input to the activation estimations and simulations of background in the experiments from proton gas scattering in the IRs.

2 Considerations

The elements of the LHC vacuum system may be classified by their operating temperature, namely 1.9 K, 4.5 K or at room temperature. Of course their exist transitions between these elements, such as interconnections and cold/warm transitions. For simplicity we assume an operating temperature of 80K in the latter case. Photon (PSD), Electron (ESD) and Ion (ISD) Stimulated Desorption and thermal desorption are potential gas sources in the LHC and all are considered here. These phenomena have been previously studied separately at both cryogenic and room temperature [4-20] and here are combined to give a general picture of the performance of the LHC vacuum system in the IRs.

In this study we assume that all the vacuum chambers at cryogenic temperatures have an actively cooled beam screen operating between 5 and 20K and that the room temperature sectors are pumped with lumped pumps separated adequately to ensure vacuum stability.

3 A model of dynamic desorption processes in a beam vacuum chamber

The equations of gas dynamic balance inside a vacuum chamber can be written as [4,5]:

$$V\frac{dn}{dt} = q + q^{\cent}(s) - aS\left(n - n_e(s,T)\right) - Cn + u\frac{d^2n}{dz^2}; \quad (1)$$

$$A\frac{ds}{dt} = aS\left(n - n_e(s,T)\right) - q^{\cent}(s); \quad (2)$$

where n *[molecules/cm^3]* is the volume gas density;

s *[molecules/cm^2]* is the surface density of cryosorbed gas;

V *[cm^3]* is the vacuum chamber volume;

A *[cm^2]* is the vacuum chamber wall area;

q *[molecules/sec]* is the primary beam induced desorption flux;

$q^{\cent}$ *[molecules/sec]* is secondary beam induced desorption flux (desorption of cryosorbed molecules);

a is the sticking coefficient;

$S = A\bar{v}/4$ is the ideal wall pumping speed, $\bar{v}$ is the mean molecular speed;

$C = r k_t S$ is the distributed pumping speed of holes, r is the capture factor for the holes, k_t is the fractional pumping slot area of the beam screen;

n_e *[molecules/cm^3]* is the thermal equilibrium gas density;

$u = A_c D$ is the specific vacuum chamber conductance per unit axial length, A_c is the vacuum chamber cross section; D is the Knudsen diffusion coefficient.

The beam induced desorption flux consist of PSD, ESD, ISD:

$$q = \eta\dot{\Gamma} + \varphi\dot{\Theta} + \kappa\frac{Is}{e}n; \qquad (3)$$

$$q' = \eta'\dot{\Gamma} + \varphi'\dot{\Theta} + \kappa'\frac{Is}{e}n;$$

where

η and η' *[molecules/photon]* are the primary and secondary photodesorption yield;

$\dot{\Gamma}$ *[photon/sec]* is the photon flux;

φ and φ' *[molecules/electron]* are the primary and secondary electron stimulated desorption yield;

$\dot{\Theta}$ *[electron/sec]* is the electron flux;

κ and κ' *[molecules/ion]* are the primary and secondary ion induced desorption yield;

I *[A]* is the proton beam current;

e is the electron charge;

s is the proton ionisation cross section of the residual gas molecules.

It was shown previously [6] that the gas density increase due to the ISD is insignificant when the beam current, I, is much less than the critical current, I_c. The vacuum stability requirement for the LHC is that, I_c/I_{ult} should not be less than 2, where I_{ult} is the ultimate current (0.85A for one beam and 1.7A for two beams in the same vacuum chamber). Assuming the recommendations from this previous study are adopted, namely the distance between lumped pumps in the room temperature regions and the beam screen with pumping slots providing an adequate distributed pumping speed in the cryogenic elements, then the ISD contribution to the gas density will be negligible [6]. It is therefore justified to neglect ISD in this study.

The solutions of equations (1) and (2) have been discussed previously [3,6]. Here we are interested in the solutions in the equilibrium state when the conditions $V\,dn/dt = 0$ and $A\,ds/dt = 0$ are satisfied. The former is reached a few milliseconds after beam injection and the latter is reached a few hours or even days after the first beam is injected, see attachment in reference [6]. These conditions provide the maximum gas density during any run of the LHC *if no gas were previously condensed* on a beam screen. This value will on the other hand be considerably higher if a significant amount of gas were pre-condensed on the inner surface of a beam screen.

The solutions to the equations (1) and (2) can be found for three distinct pumping configurations employed in the LHC and are given below. Consider a vacuum chamber of length L, centred at $z = 0$, then the following solutions are used:

a) For an infinitely long vacuum chamber with distributed pumping, such as in the arcs and DS with a beam screen with pumping slots:

$$n = \frac{q}{C}. \tag{4}$$

b) For a finite length vacuum chamber with distributed pumping between two pumps with a pumping speed S_p, such as the quadrupoles Q4-Q6 with a beam screen with pumping in stand-alone cryostats:

$$n(z) = \frac{q}{C}\left(1 - \frac{\tanh\left(\sqrt{\frac{C}{u}}\frac{L}{2}\right)}{\sqrt{\frac{C}{u}}\frac{L}{2}\left(1 + \frac{\sqrt{Cu}}{S_p}\tanh\left(\sqrt{\frac{C}{u}}\frac{L}{2}\right)\right)}\right). \tag{5}$$

c) For a finite length vacuum chamber without distributed pumping between two pumps with a pumping speed S_p, such as the room temperature vacuum chambers:

$$n(z) = \frac{q}{2u}\left(\frac{L^2}{4} - z^2\right) + \frac{qL}{2S_p}. \tag{6}$$

It should be noted that these solutions depend only on the primary desorption, q, *i.e.* there is no dependence on the secondary desorption, q'. Hence, the gas density depends only on primary PSD and ESD.

A detailed study of the sources of synchrotron radiation (SR) in the LSSs is presented as an annex to this paper. In the following sections PSD and ESD input data are described. These are used in section 5 to estimate the dynamic gas densities in the LSSs.

3.1 Photon stimulated desorption

The photon flux is proportional to the beam current, $\dot{\Gamma} \propto I$, and hence the PSD flux is also proportional to the beam current:

$$Q_{ph} = h(e_c, \Gamma)\dot{\Gamma}(I), \quad \text{i.e.} \; Q_{ph} \propto I. \tag{7}$$

The PSD yields have been studied at CERN and other research centres. In the estimations presented here the PSD yields at room temperature for an *in-situ* baked (150°C, 24 hrs.) OFE Cu vacuum chamber [7,8], an *in-situ* baked (350°C) Cu-lined SS vacuum chamber [9] and for an unbaked Cu-lined SS vacuum chamber at cryogenic temperatures [10] were used. The PSD yield, h, decreases with photon dose proportionally to $\dot{\Gamma}^{-a}$. Both the initial PSD yield and the power a in $\dot{\Gamma}^{-a}$ are higher at higher temperatures [11]. At room temperature $a \approx 2/3$ [7,8,11] while $a \approx 1/3$ at 78 K [10,11] and $a \approx 0.1$ at 4.2 K [4,9,11]. The PSD yields as function of photon dose at room temperature and at 78 K are shown in Figure 1 (a) and Figure 3 (a) respectively. Assuming 20% of nominal beam current the dose can be converted to operation time of the LHC gas (Figure 1 (b) and Figure 3 (b)). The same data can be converted to the dependence of PSD yields as function of the amount of desorbed gas (see Figure 1 (c) and Figure 3 (c)).

3.2 Electron stimulated desorption

The energy of electrons, E_e, bombarding the vacuum chamber increases with the proton beam current, I, due to Beam Induced Electron Multipacting (BIEM) and reaches an average energy of few hundred eV at the nominal beam current [12,13,14]. The ESD yield increases with the impact electron energy between a few eV and 2000 eV [15]. The ESD flux is:

$$Q_e = f(E_e(I), \Theta)\dot{\Theta}(E_e(I)), \quad \text{i.e.} \; Q_e \propto I^z \; \text{with} \; 1 < z \leq 2; \tag{8}$$

where f is the ESD yield and $\dot{\Theta}$ is the flux of electrons. Hence, the ESD is more sensitive to the beam current than the PSD flux.

The power that may be removed from the arc beam screen is given by the installed cryogenic capacity and is limited to 1.17 W/m. A reasonable average cryogenic heat load from BIEM is estimated

to be of the order of 200 mW/m [16]. If the beam parameters are such that the heat load from the electron cloud corresponds to W = 200 mW/m, then $\dot{\Theta} = W/E_e(I)$. For $f \mu E_e(I)$ we have

$$Q_e = f\dot{\Theta} = (k \times E_e) \times \left(\frac{W}{E_e}\right) = k \times W, \tag{9}$$

where k is a constant, i.e. the ESD flux is proportional to the total power deposited by the electrons.

The ESD yield as a function of electron dose were studied previously [16,17,18,19]. The initial ESD yields as function of baking from 200°C to 600°C for 24 hrs was also studied [20]. These different data are found to be in reasonable agreement taking into account the effect of electron energy, sample preparation, dependence of baking temperature, *etc*. For these estimations the most recent data [18] were used. The reduction of ESD yield after baking at 300°C for 24 hrs is a factor 10 for H_2 and a factor 20 for CH_4, CO and CO_2. The ESD yields at room temperature are shown in Figure 2 as function of the electron dose and the amount of desorbed gas.

The ESD yields for an unbaked vacuum chamber at low temperatures (between 3 and 77 K) can differ from those presented in Figure 2. Meanwhile, in the absence of any data on ESD yields from a surface at low temperature, the ESD yields at low temperature were estimated using:

$$f_{cryo} = h_{cryo} \times \frac{f_{RT}}{h_{RT}}. \tag{10}$$

i.e. it is assumed that the ratio h/f for each gas is preserved at room temperature and at cryogenic temperatures.

The ESD yields at 78 K are shown in Figure 4 as function of electron dose and the amount of desorbed gas. The dependence of time corresponds to the BIEM power of 200 mW/m.

It is important to note that a quadrupole or solenoid magnetic field will attenuate the effect of BIEM and, hence, also the ESD.

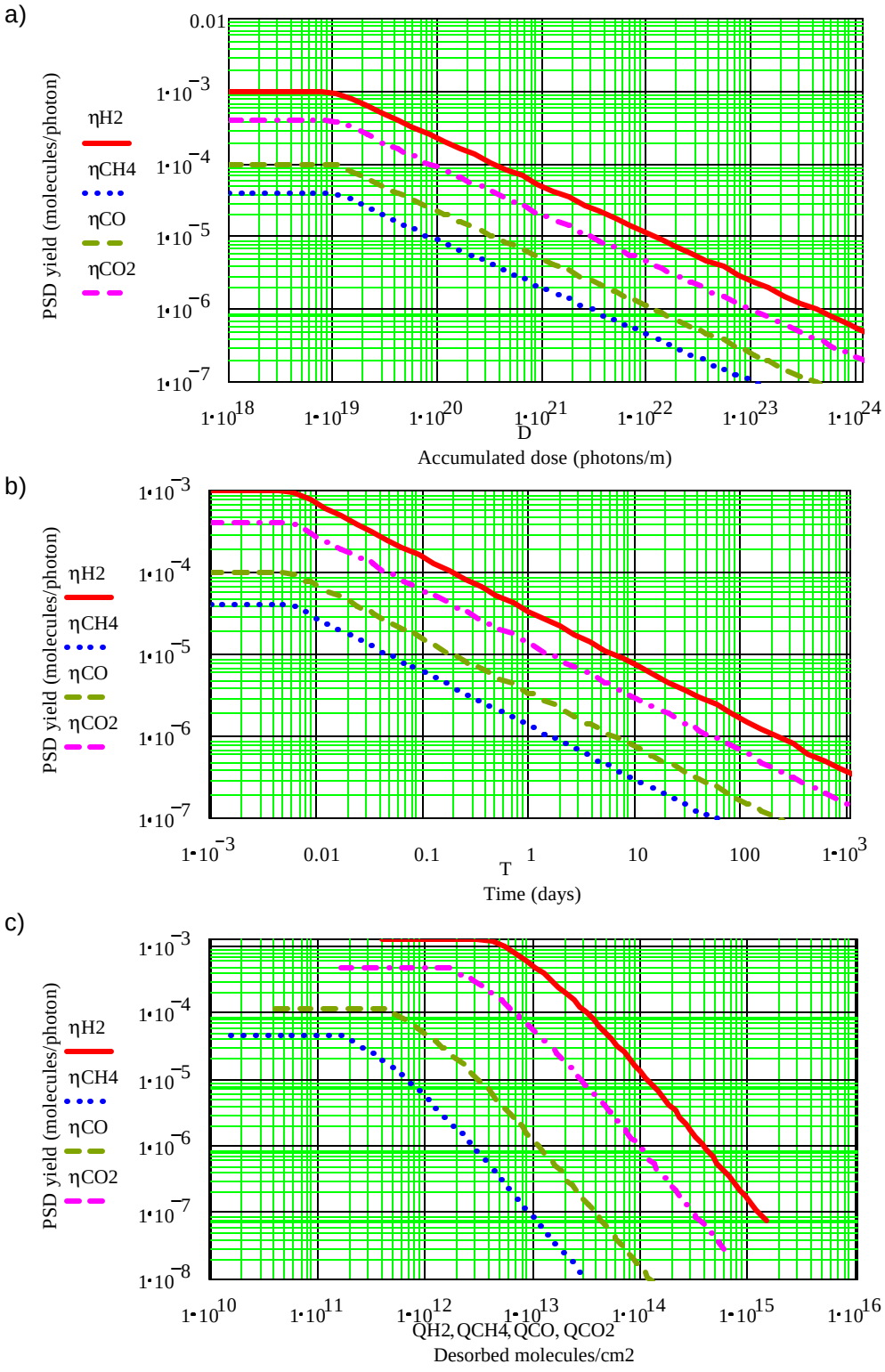

Figure 1. PSD yield at E_c»50 eV for a RT OFE Cu-lined SS vacuum chamber baked *in-situ* at 300°C for 24 hrs as a function of a) accumulated photons, b) time with 2×10^{16} photon/m i.e. I=0.2I_n and c) desorbed molecules.

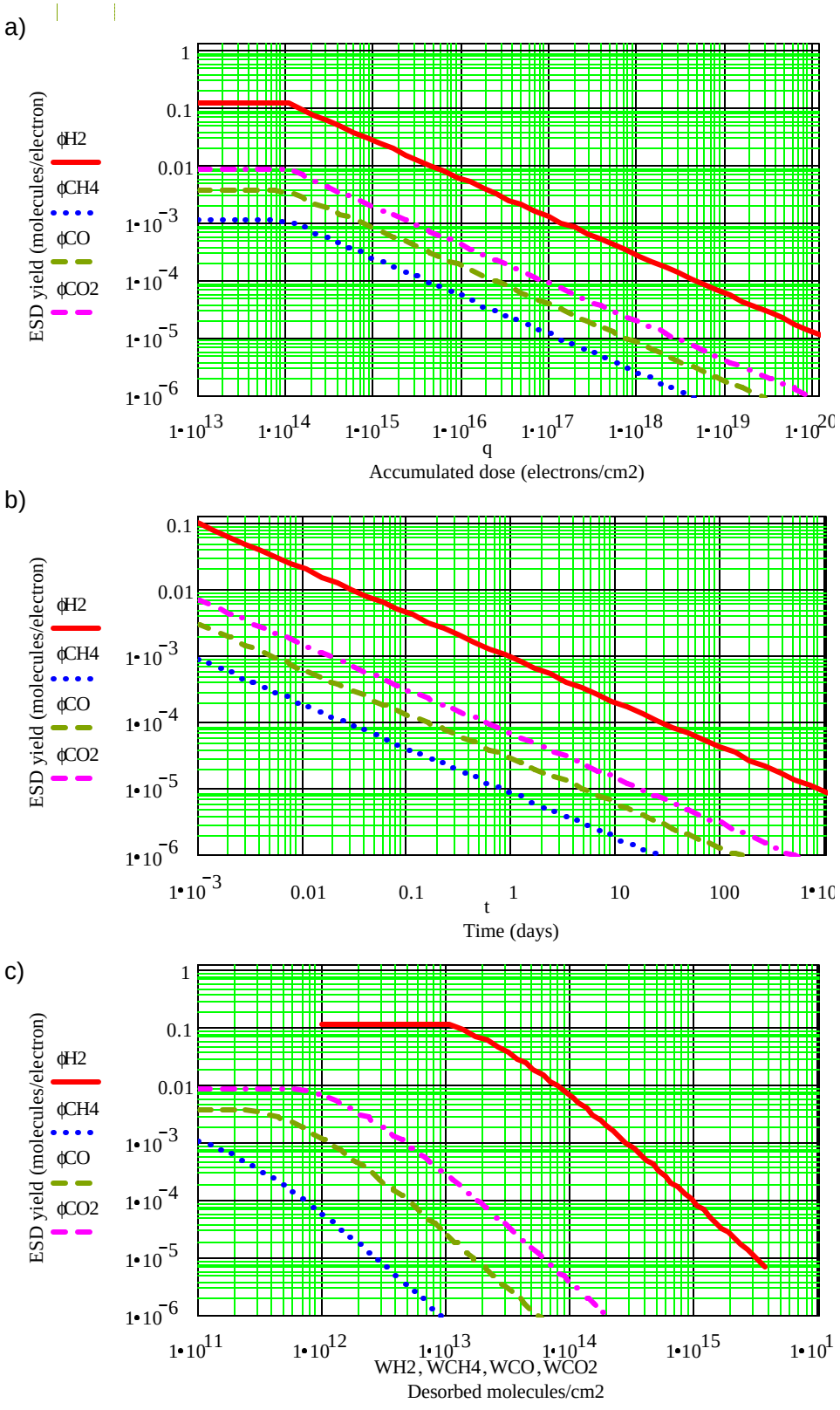

Figure 2. ESD yield at E_e=300 eV for a RT OFE Cu-lined SS vacuum chamber baked *in-situ* at 300 °C for 24 hrs as a function of: a) accumulated electrons, b) time at W=0.2W/m and desorbed molecules.

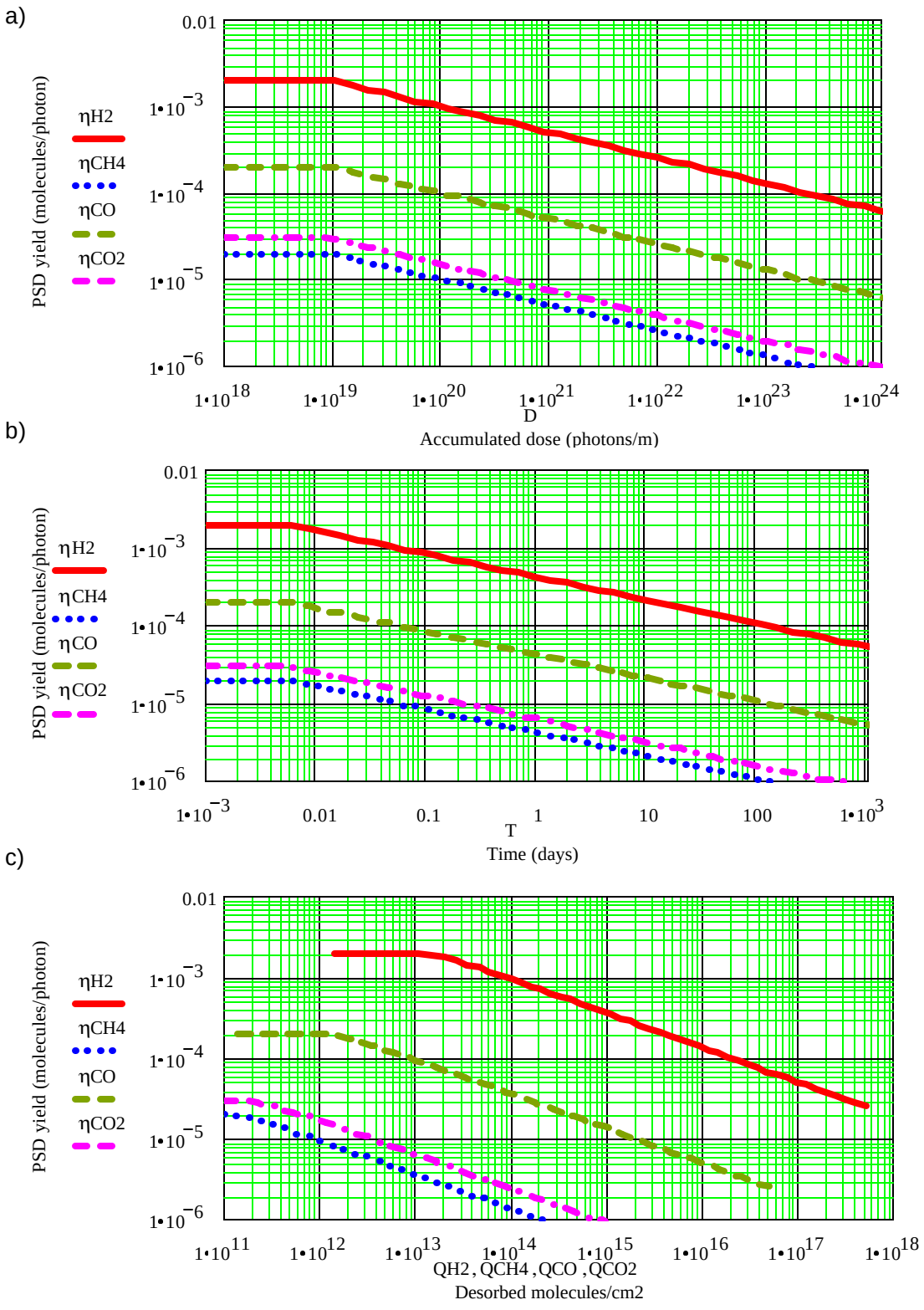

Figure 3. PSD yield at E_c» 50 eV for an unbaked OFE Cu-lined SS vacuum chamber at 78 K as a function of: a) accumulated photons, b) time with 2‹10^{16} photon/m i.e. I=0.2I_n and c) desorbed molecules.

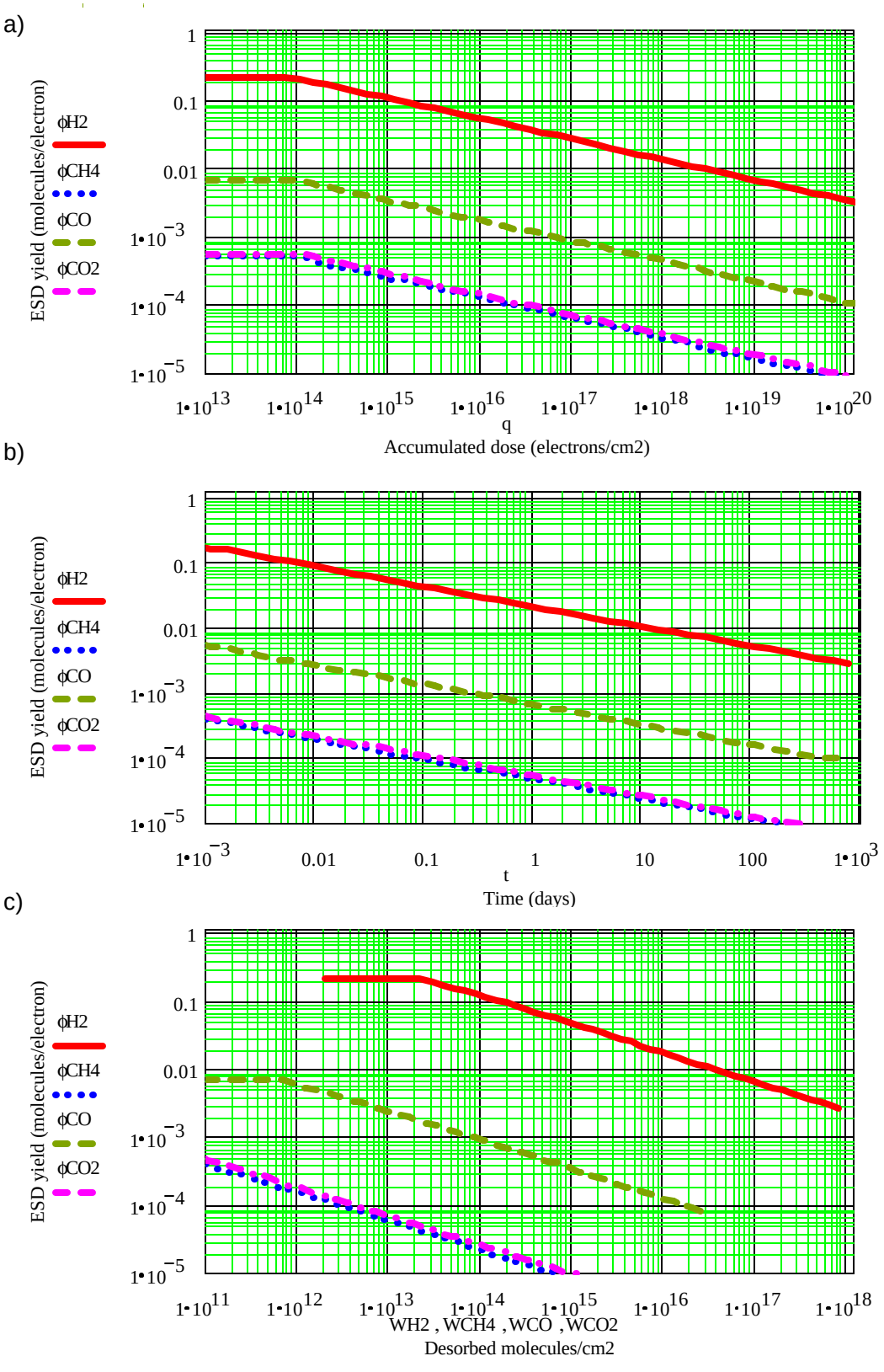

Figure 4. ESD yield at E_e=300 eV for an unbaked OFE Cu-lined SS vacuum chamber at 78 K as a function of: a) accumulated electrons, b) time at W=0.2W/m and c) desorbed molecules.

4 A machine operation scenario

4.1 First year operation, $I < 0.3\ I_n$.

A proposed start-up scenario for LHC in the first year is a run for about 10 weeks with a low beam current [21], where BIEM should be negligible [22]. Hence, during this time the LHC gas density will be dominated by PSD. The corresponding photon flux for 20% of the nominal current, I_n, in the arcs and DS will be $2 \cdot 10^{16}$ photons/(s·m). This 70 day operation corresponds to an accumulated photon dose of $1.2 \cdot 10^{23}$ photons/m in the arcs. This corresponds to a reduction in the PSD yield, due to photon conditioning, of about a factor 15 for the vacuum chambers in the arcs and DS (see Figure 4a).

In the LSS the photon flux and critical energy of SR are smaller than that that in the arcs (see annex). The corresponding accumulated photon dose and therefore the photon conditioning for the elements of the LSS vacuum chambers will be less. For the cryogenic elements in Ring 1 the photon conditioning factors are 12 for Q7, 7 for Q6, 5 for Q5 and 4 for Q4. It is important to note that the dipole D2 may not be irradiated due to the shadow cast by smaller inner diameter of the upstream Q4. For the room temperature vacuum chambers the photon conditioning factor is a 100 between Q6 and Q7, 50 between Q5 and Q6 and 25 between Q4 and Q5. In Ring 2 the photon conditioning factors are always less than in Ring 1 due to the lower photon flux from D2 and the lower photon critical energy. Moreover there are locations of room temperature vacuum chamber shadowed from SR, such as after each cold-warm transition due to the change of vacuum chamber diameter. Conversely at the warm/cold transition the vacuum will be irradiated by photons with higher intensity (see Table 8). Thus the photon conditioning factor in LSS will vary between 1 and 15 and between 1 and 100 in the room temperature vacuum chambers depending on their location.

4.2 Following years operation, $0.3 \leq I_n \leq I_n$.

Following the estimations of F. Zimmerman *et al*. BIEM will be significant at about 30% of nominal beam intensity [22]. Since it is difficult to predict the exact power generated by the electron cloud we use the value of 200 mW/m as an initial power (see section 3.2). The final value of BIEM power deposited in an arc dipole magnet at nominal beam current after a long conditioning time is expected to be ~ 40 mW/m [22].

In order to estimate the initial ESD yield after the photon conditioning in the first year we assume that both PSD and ESD yields are directly correlated to the quantity of gas desorbed. In other words the quantity of gas removed from the vacuum chamber walls due to the PSD in the first year then defines the initial ESD yields.

During the 70 day operation in the first year the accumulated photon dose in the arcs and DS will be $1.2 \cdot 10^{23}$ photons/m. By comparing the dependencies of PSD and ESD yields with the quantity of desorbed gas (see Figure 3 and Figure 4) one can see that the conditioning factors in ESD and PSD for cryogenic vacuum chambers are about the same for the same quantity of gas desorbed. The effect of the 70 days photon conditioning in the arcs and DS corresponds to about one to two days of the operation in a regime with a BIEM heat load of 200 mW/m. After 10 days conditioning with electrons the preconditioning with photons will be insignificant.

This situation is somewhat different in the room temperature vacuum chambers. For example, the non-shadowed part of the vacuum chambers between Q6 and Q7 of LSS1&5, which will be most intensively irradiated of all room temperature vacuum chambers, will desorb about 10^{14} H_2/cm^2 (see Figure 1), the PSD yield will be reduced by a factor of 100. During this photon conditioning the initial ESD yield will only reduce by a factor of 20 (see Figure 2). Hence, the conditioning factor for ESD in the RT vacuum chambers of the LSS is much less than that for PSD. Since some of the RT vacuum chamber in LSS have a shadowed part there exist places where there will be no photon conditioning. Meanwhile from Figure 2 one can see that the conditioning is very efficient in the presence of BIEM; the ESD yield reduces more than factor 25 during 1 day and a factor of 100 during 10 days operation with a BIEM heat load of 200 mW/m.

It is also necessary to note that BIEM will not occur simultaneously around the machine. First it will manifest in the arcs and DS resulting in an increased gas density. Once conditioned the machine

current or bunch density may be increased. BIEM may then become significant in other regions of the machine, such as in vacuum chambers with larger inner diameters in dipole fields and/or field free regions, resulting in a gas density increase in these locations. This effect will be repeated until the nominal or ultimate machine parameters are reached or all the vacuum system has been conditioned by BIEM.

5 Inputs and results

The cryogenic elements of the machine shall be equipped with actively cooled and thermally controlled screens that provide distributed pumping of all gases thereby ensuring vacuum stability [6]. The transparency of all such screens is assumed to be 4.4%, that of the arc beam screen, with a capture factor of 0.5 for H_2 and 0.65 for other gases [23].

In the room temperature sections of the machine the lumped pumping (sputter ion pumps and Ti sublimation pumps with a 200 l/s nitrogen equivalent pumping speed [24]) is assumed. These pumps are located at every cold/warm transition and according to vacuum stability requirements [6], *i.e.* these pumps are foreseen to be located every 7 m for the standard ID 80 mm drift chambers.

The gas composition in a vacuum system, required to calculate the backgrounds to the detectors, is strongly related to the temperature of the vacuum chamber, *via* the temperature dependence of the desorption yields and the molecular conductance of the gases (pumping speed), and is presented in Table 1. A range of values in the gas composition at room temperature is given to reflect the scatter in the experimental data from OFHC Cu reported by various different research groups and the observed changes with dose. The gas densities are related to both lifetime limit and background for experiments *via* the total nuclear scattering cross section, σ. The relative nuclear scattering cross sections with respect to H_2, σ_i/σ_{H2} at 7 TeV derived in [25] are also shown in Table 1.

Table 1. The gas composition in the elements of the LHC and the relative nuclear scattering cross sections with respect to H_2.

Gas	σ_i/σ_{H2}	RT vacuum chamber	Cryogenic vacuum chamber
H_2	1	~30–50%	~99%
CH_4	5.4	~2%	0.04%
CO	7.8	~10–15%	0.5%
CO_2	12.2	~40–50%	0.03%

The estimations are made for each element of the vacuum chamber and the results are presented in the form of an *effective* H_2 equivalent average gas density, given by:

$$< n_{eff} >= n(H_2) + 5.4n(CH_4) + 7.8n(CO) + 12.2n(CO_2). \quad (11)$$

The variations of the gas composition indicated in Table 1 affects the resulting effective gas density, $< n_{eff} >$, by only $\pm 5\%$ and is therefore insignificant when compared to the factor of two uncertainty in the input data.

5.1 IR1 and IR5

Since the optics layouts of LSS1 and LSS5 are identical and symmetric about their IP, apart from the slope of the machine, it is convenient to consider only one side. A schematic of the optics version 6.3 of LSS1 lhs is shown in Figure 5.

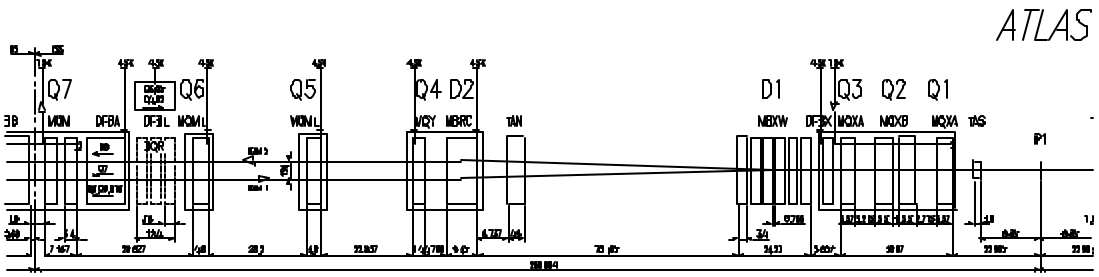

Figure 5. Schematic of the LSS lhs in IR1 and IR5.

The vacuum chambers between D1 and TAN consist of two elements with ID = 164 mm and ID =212 mm and with L $\approx$ 38 m each and with pumps every 7 m, no BIEM are foreseen in these vacuum chambers [26].

The estimated average H_2 equivalent gas densities at various times for the assumed operational scenario of the machine are presented in Table 2. (RT) identifies elements at room temperature, all others are at cryogenic temperatures. Values greater than 10^{15} molecules/m^3, the beam lifetime limit, are highlighted in bold.

Table 2. The H_2 equivalent average gas density in the vacuum chamber of the IR1&5.

Element	L, (m)	$<n_{eff}>$ (mol/m^3),				
		1st year		2nd year		3rd year
		beginning $I = 0.2\ I_n$, $W_e=0$	after 70 days $I = 0.2\ I_n$, $W_e=0$	beginning $I \sim 0.3\ I_n$, $W_e=0.2$W/m	+10 days $I \sim 0.3\ I_n$, $W_e=0.2$W/m	+90 days $I = I_n$, $W_e=40$mW/m
Intercon	0.83	$1.5{\cdot}10^{14}$	$2{\cdot}10^{13}$	$\mathbf{2{\times}10^{15}}$	$2{\cdot}10^{14}$	$1{\cdot}10^{14}$
Q1	7.70	$2{\cdot}10^{13}$	$3{\cdot}10^{12}$	$5{\cdot}10^{13}$	$8{\cdot}10^{12}$	$6{\cdot}10^{12}$
Intercon.	1.40	$2{\cdot}10^{13}$	$3{\cdot}10^{12}$	$\mathbf{3{\times}10^{15}}$	$3{\cdot}10^{14}$	$1.5{\cdot}10^{14}$
Q2	12.58	$2{\cdot}10^{13}$	$3{\cdot}10^{12}$	$3{\cdot}10^{13}$	$5{\cdot}10^{12}$	$3{\cdot}10^{12}$
Intercon.	1.90	$2{\cdot}10^{13}$	$3{\cdot}10^{12}$	$\mathbf{3{\times}10^{15}}$	$3{\cdot}10^{14}$	$1.5{\cdot}10^{14}$
Q3	8.40	$2{\cdot}10^{13}$	$3{\cdot}10^{12}$	$5{\cdot}10^{13}$	$8{\cdot}10^{12}$	$6{\cdot}10^{12}$
DFBX	3.23	$2{\cdot}10^{13}$	$3{\cdot}10^{12}$	$\mathbf{3{\times}10^{15}}$	$3{\cdot}10^{14}$	$1.5{\cdot}10^{14}$
D1 (RT)	~25	$\mathbf{1{\times}10^{15}}$	$2{\cdot}10^{13}$	$\mathbf{6{\times}10^{16}}$	$6{\cdot}10^{14}$	$5{\cdot}10^{12}$
'Conus' (RT)	~57	$\sim10^{12}$	$\sim10^{12}$	$\sim10^{12}$	$\sim10^{12}$	$\sim10^{12}$
TAN (RT)	4.9	$\mathbf{1{\times}10^{16}}$	$1{\cdot}10^{14}$	$\mathbf{9{\times}10^{16}}$	$8{\cdot}10^{14}$	$7{\cdot}10^{12}$
Ring 1. The beam from MB to IP.						
VC (RT)	7.50	$3{\cdot}10^{14}$	$1{\cdot}10^{13}$	$\mathbf{7{\times}10^{16}}$	$6{\cdot}10^{14}$	$5{\cdot}10^{12}$
D2	11.67	$<10^{12}$	$<10^{12}$	$\mathbf{6{\times}10^{15}}$	$3{\cdot}10^{14}$	$1.5{\cdot}10^{14}$
Q4	8.65	$3{\cdot}10^{12}$	$9{\cdot}10^{11}$	$6{\cdot}10^{14}$	$4{\cdot}10^{13}$	$2{\cdot}10^{13}$
VC (RT)	19.38	$\mathbf{1{\times}10^{15}}$	$\sim10^{12}$	$\mathbf{6{\times}10^{16}}$	$6{\cdot}10^{14}$	$5{\cdot}10^{12}$
Q5	8.25	$6{\cdot}10^{12}$	$1.2{\cdot}10^{12}$	$5{\cdot}10^{14}$	$4{\cdot}10^{13}$	$2{\cdot}10^{13}$
VC (RT)	24.76	$\mathbf{2{\times}10^{15}}$	$2{\cdot}10^{13}$	$\mathbf{6{\times}10^{16}}$	$6{\cdot}10^{14}$	$5{\cdot}10^{12}$
Q6	8.25	$1.5{\cdot}10^{13}$	$2{\cdot}10^{12}$	$4{\cdot}10^{14}$	$4{\cdot}10^{13}$	$2{\cdot}10^{13}$
VC (RT)	17.73	$\mathbf{4{\times}10^{15}}$	$2.5{\cdot}10^{13}$	$\mathbf{6{\times}10^{16}}$	$6{\cdot}10^{14}$	$5{\cdot}10^{12}$
DFBA	8.58	$7{\cdot}10^{13}$	$7{\cdot}10^{13}$	$6{\cdot}10^{14}$	$3{\cdot}10^{14}$	$1.5{\cdot}10^{14}$
Q7	9.00	$1.5{\cdot}10^{14}$	$1.2{\cdot}10^{13}$	$1.8{\cdot}10^{13}$	$1.6{\cdot}10^{13}$	$2{\cdot}10^{13}$
DS&Arcs		$2{\cdot}10^{14}$	$1{\cdot}10^{13}$	$1.5{\cdot}10^{14}$	$3{\cdot}10^{13}$	$4{\cdot}10^{12}$
Ring 2. The beam from IP to MB.						
VC (RT)	7.50	$<10^{12}$	$<10^{12}$	$\mathbf{7{\times}10^{16}}$	$6{\cdot}10^{14}$	$5{\cdot}10^{12}$
D2	11.67	$<10^{12}$	$<10^{12}$	$\mathbf{6{\times}10^{15}}$	$3{\cdot}10^{14}$	$1.5{\cdot}10^{14}$
Q4	8.65	$<10^{12}$	$<10^{12}$	$6{\cdot}10^{14}$	$4{\cdot}10^{13}$	$2{\cdot}10^{13}$
VC (RT)	19.38	$\mathbf{1{\times}10^{15}}$	$\sim10^{12}$	$\mathbf{6{\times}10^{16}}$	$6{\cdot}10^{14}$	$5{\cdot}10^{12}$
Q5	8.25	$3{\cdot}10^{12}$	$1.2{\cdot}10^{12}$	$5{\cdot}10^{14}$	$4{\cdot}10^{13}$	$2{\cdot}10^{13}$
VC (RT)	24.76	$8{\cdot}10^{14}$	$1{\cdot}10^{13}$	$\mathbf{6{\times}10^{16}}$	$6{\cdot}10^{14}$	$5{\cdot}10^{12}$
Q6	8.25	$2{\cdot}10^{12}$	$1{\cdot}10^{12}$	$5{\cdot}10^{14}$	$4{\cdot}10^{13}$	$2{\cdot}10^{13}$
VC (RT)	17.73	$5{\cdot}10^{14}$	$1{\cdot}10^{13}$	$\mathbf{6{\times}10^{16}}$	$6{\cdot}10^{14}$	$5{\cdot}10^{12}$
DFBA	8.58	$2{\cdot}10^{12}$	$1{\cdot}10^{12}$	$6{\cdot}10^{14}$	$3{\cdot}10^{14}$	$1.5{\cdot}10^{14}$
Q7	9.00	$2{\cdot}10^{12}$	$1{\cdot}10^{12}$	$1.8{\cdot}10^{13}$	$1.6{\cdot}10^{13}$	$2{\cdot}10^{13}$
DS	171.4	$2{\cdot}10^{14}$	$1{\cdot}10^{13}$	$7{\cdot}10^{14}$	$3{\cdot}10^{13}$	$4{\cdot}10^{12}$
Arcs		$2{\cdot}10^{14}$	$1{\cdot}10^{13}$	$1.5{\cdot}10^{14}$	$3{\cdot}10^{13}$	$4{\cdot}10^{12}$

5.2 IR2 and IR8

The optics layouts of LSS2 rhs and LSS8 lhs as well as LSS2 lhs and LSS8 rhs are identical but not symmetric about the IP.

A schematic of the optics version 6.3 of LSS2 is shown in Figure 6.

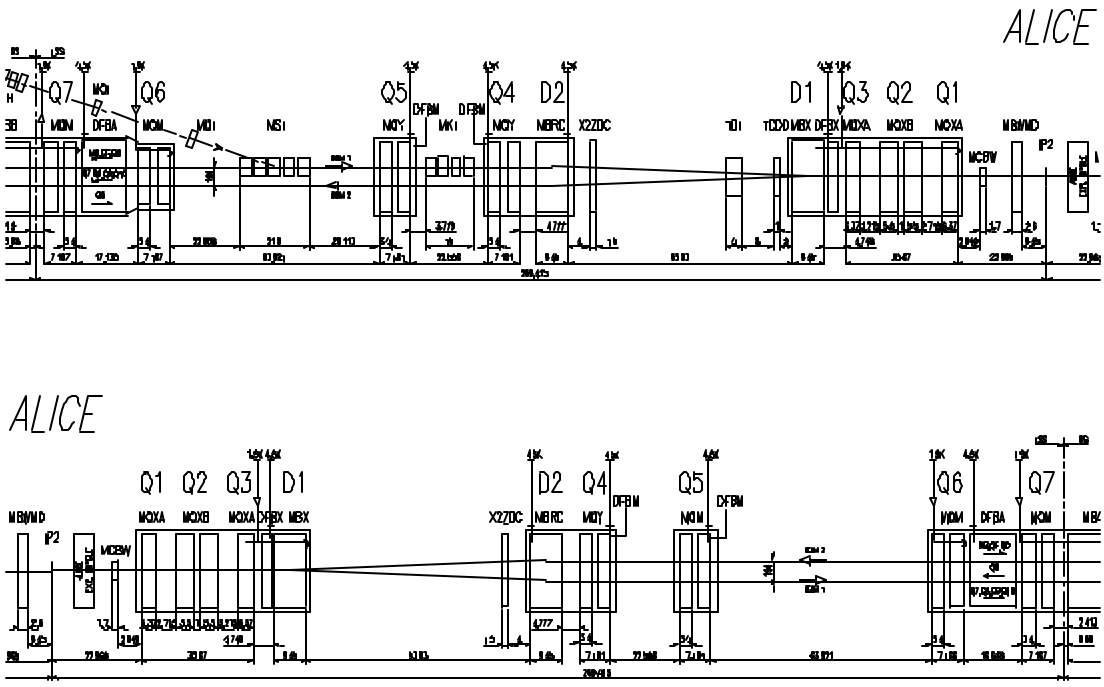

Figure 6. Schematic of the LSS in IR2.

The gas density in the TDI is estimated in the retracted position, *i.e.* after injection. For the estimations a thermal outgassing rate of 10^{-9} Torr·l/s·cm^2 for graphite, type SGL1501 G (Carbon-Carbon composite proposed for the TDI), after an *in-situ* bake-out at 200 to 250 °C for several days is assumed. In addition an installed pumping speed of 3600l/s [27], neglecting the restricted conductance of the screen pumping, is assumed.

The vacuum chambers between D1 and D2 consist of a number of inner diameter tubes between 206 mm and 600 mm and with lengths between pumps between 5 m and 8 m [28]. No

significant BIEM is foreseen in these vacuum chambers. The largest diameter vacuum chamber, closest to D2, is connected to a recombination vacuum chamber (Y-type chamber). This chamber makes a smooth transition from one vacuum chamber for both beams to two separate vacuum chambers for each beam. In IR2 this vacuum chamber is compatible with the Zero Degree Calorimeter (X2ZDC).

The estimated average H_2 equivalent gas densities at various times for the assumed operational scenario of the machine are presented in Table 3. (RT) identifies elements at room temperature, all others are at cryogenic temperatures. Values greater than 10^{15} molecules/m^3, the beam lifetime limit, are highlighted in bold.

Table 3. The H_2 equivalent average gas density in the vacuum chamber of the IR2&8.

Element	L, (m)	$<n_{eff}>$ (mol/m^3),				
		1st year		2nd year		3rd year
		beginning $I = 0.2\ I_n$, $W_e=0$	after 70 days $I = 0.2\ I_n$, $W_e=0$	beginning $I \sim 0.3\ I_n$, $W_e=0.2$W/m	+10 days $I \sim 0.3\ I_n$, $W_e=0.2$W/m	+90 days $I = I_n$, $W_e=40$mW/m
Intercon	0.83	$1.5{\cdot}10^{14}$	$2{\cdot}10^{13}$	$\mathbf{2{\times}10^{15}}$	$2{\cdot}10^{14}$	$1{\cdot}10^{14}$
Q1	7.70	$2{\cdot}10^{13}$	$3{\cdot}10^{12}$	$5{\cdot}10^{13}$	$8{\cdot}10^{12}$	$6{\cdot}10^{12}$
Intercon.	1.40	$2{\cdot}10^{13}$	$3{\cdot}10^{12}$	$\mathbf{3{\times}10^{15}}$	$3{\cdot}10^{14}$	$1.5{\cdot}10^{14}$
Q2	12.58	$2{\cdot}10^{13}$	$3{\cdot}10^{12}$	$3{\cdot}10^{13}$	$5{\cdot}10^{12}$	$3{\cdot}10^{12}$
Intercon.	1.90	$2{\cdot}10^{13}$	$3{\cdot}10^{12}$	$\mathbf{3{\times}10^{15}}$	$3{\cdot}10^{14}$	$1.5{\cdot}10^{14}$
Q3	8.40	$2{\cdot}10^{13}$	$3{\cdot}10^{12}$	$5{\cdot}10^{13}$	$8{\cdot}10^{12}$	$6{\cdot}10^{12}$
DFBX	3.23	$2{\cdot}10^{13}$	$3{\cdot}10^{12}$	$\mathbf{3{\times}10^{15}}$	$3{\cdot}10^{14}$	$1.5{\cdot}10^{14}$
D1	11.36	$2{\cdot}10^{13}$	$3{\cdot}10^{12}$	$\mathbf{3{\times}10^{15}}$	$3{\cdot}10^{14}$	$1.5{\cdot}10^{14}$
TDI (RT)	5.0	$\mathbf{\sim 10^{16}}$	$\mathbf{\sim 10^{16}}$	$\mathbf{\sim 10^{16}}$	$\mathbf{\sim 10^{16}}$	$\mathbf{\sim 10^{16}}$
conus (RT)	47.07	$\sim 10^{12}$	$\sim 10^{12}$	$\sim 10^{12}$	$\sim 10^{12}$	$\sim 10^{12}$
XZDC (RT) in IR2	1.50	$\mathbf{3{\times}10^{15}}$	$1{\cdot}10^{14}$	$1.5{\cdot}10^{14}$	$5{\cdot}10^{13}$	$\sim 10^{12}$
Y (RT) in IR8	1.0	$\mathbf{1{\times}10^{16}}$	$1{\cdot}10^{14}$	$\mathbf{9{\times}10^{16}}$	$8{\cdot}10^{14}$	$7{\cdot}10^{12}$
Ring 1. The beam from MB to IP.						
VC (RT)	4.0	$<10^{12}$	$<10^{12}$	$\mathbf{7{\times}10^{16}}$	$6{\cdot}10^{14}$	$5{\cdot}10^{12}$
D2	11.67	$<10^{12}$	$<10^{12}$	$\mathbf{6{\times}10^{15}}$	$3{\cdot}10^{14}$	$1.5{\cdot}10^{14}$
Q4	12.50	$3{\cdot}10^{12}$	$9{\cdot}10^{11}$	$6{\cdot}10^{14}$	$4{\cdot}10^{13}$	$2{\cdot}10^{13}$
VC (RT)	16.75	$\mathbf{1{\times}10^{15}}$	$<10^{12}$	$\mathbf{6{\times}10^{16}}$	$6{\cdot}10^{14}$	$5{\cdot}10^{12}$
Q5	12.99	$3{\cdot}10^{12}$	$9{\cdot}10^{11}$	$6{\cdot}10^{14}$	$4{\cdot}10^{13}$	$2{\cdot}10^{13}$
VC (RT)	60.96	$\mathbf{3{\times}10^{15}}$	$1{\cdot}10^{13}$	$\mathbf{6{\times}10^{16}}$	$6{\cdot}10^{14}$	$5{\cdot}10^{12}$
Q6	10.36	$3{\cdot}10^{13}$	$2{\cdot}10^{12}$	$4{\cdot}10^{14}$	$4{\cdot}10^{13}$	$2{\cdot}10^{13}$
DFBA	14.7	$1{\cdot}10^{14}$	$7{\cdot}10^{13}$	$6{\cdot}10^{14}$	$3{\cdot}10^{14}$	$1.5{\cdot}10^{14}$
Q7	9.00	$1.5{\cdot}10^{14}$	$1.2{\cdot}10^{13}$	$1.8{\cdot}10^{13}$	$1.6{\cdot}10^{13}$	$2{\cdot}10^{13}$
DS&Arcs		$2{\cdot}10^{14}$	$1{\cdot}10^{13}$	$1.5{\cdot}10^{14}$	$3{\cdot}10^{13}$	$4{\cdot}10^{12}$
Ring 2. The beam from IP to MB.						
VC (RT)	4.0	$<10^{12}$	$<10^{12}$	$\mathbf{7{\times}10^{16}}$	$6{\cdot}10^{14}$	$5{\cdot}10^{12}$
D2	11.67	$<10^{12}$	$<10^{12}$	$\mathbf{6{\times}10^{15}}$	$3{\cdot}10^{14}$	$1.5{\cdot}10^{14}$
Q4	12.50	$3{\cdot}10^{12}$	$9{\cdot}10^{11}$	$6{\cdot}10^{14}$	$4{\cdot}10^{13}$	$2{\cdot}10^{13}$
VC (RT)	16.75	$\mathbf{2{\times}10^{15}}$	$\sim 10^{12}$	$\mathbf{6{\times}10^{16}}$	$6{\cdot}10^{14}$	$5{\cdot}10^{12}$
Q5	12.99	$3{\cdot}10^{12}$	$1.2{\cdot}10^{12}$	$5{\cdot}10^{14}$	$4{\cdot}10^{13}$	$2{\cdot}10^{13}$
VC (RT)	60.96	$2{\cdot}10^{14}$	$1{\cdot}10^{13}$	$\mathbf{6{\times}10^{16}}$	$6{\cdot}10^{14}$	$5{\cdot}10^{12}$
Q6	10.36	$2{\cdot}10^{12}$	$1{\cdot}10^{12}$	$5{\cdot}10^{14}$	$4{\cdot}10^{13}$	$2{\cdot}10^{13}$
DFBA	14.7	$1{\cdot}10^{14}$	$1{\cdot}10^{12}$	$6{\cdot}10^{14}$	$3{\cdot}10^{14}$	$1.5{\cdot}10^{14}$
Q7	9.00	$1{\cdot}10^{14}$	$1{\cdot}10^{12}$	$1.8{\cdot}10^{13}$	$1.6{\cdot}10^{13}$	$2{\cdot}10^{13}$
DS	170.4	$2{\cdot}10^{14}$	$1{\cdot}10^{13}$	$7{\cdot}10^{14}$	$3{\cdot}10^{13}$	$4{\cdot}10^{12}$
Arcs		$2{\cdot}10^{14}$	$1{\cdot}10^{13}$	$1.5{\cdot}10^{14}$	$3{\cdot}10^{13}$	$4{\cdot}10^{12}$

5.3 Discussion

In Table 2 and **Table 3** it can be seen that in the first year, with a bunch density of < 20%, the initial gas density in the arc will be within the beam lifetime limit. All elements at cryogenic temperature shall remain below 10^{15} molecules/m^3 thanks, in part, to the distributed pumping provided by the installed beam screens. In only a few of the room temperature vacuum chambers in the LSS shall the gas density initially exceed 10^{15} molecules/m^3. The highest initial gas densities are predicted to be in the TAN in IR1&5 (10^{16} molecules/m^3), at the X2ZDC in IR2 ($3{\cdot}10^{15}$ molecules/m^3), in the recombination chambers in IR2 and IR8 (10^{16} molecules/m^3) and the TDI in IR2 lhs and IR8 rhs (10^{16} molecules/m^3). It should be noted that these elevated gas densities will however not affect the beam lifetime since it is determined by the average machine gas density. These elevated gas densities are due to the high photon fluxes intercepted by these chambers except for the TDI that is dominated by thermal out-gassing. The gas density in the TDI can be improved significantly by a judicious choice of materials and design; out-gassing rates of various graphite types can vary over three orders of magnitude! After 70 days operation under these conditions the vacuum system shall improve significantly with the highest gas density in the order of 10^{14} molecules/m^3; the exception being the TDI. Hence the performance of the beam vacuum system is expected to be quite acceptable in the first year.

Once BIEM becomes significant ESD is anticipated and the gas density will increase. In the arcs the gas density is expected to remain below the beam lifetime limit. However a BIEM induced gas density rise in the range of 10^{16} molecules/m^3 in the field free regions and in the D1 and D2 dipole fields are predicted. Such gas densities may affect the beam lifetime and may cause magnet quenches and/or background to the experiments. Fortunately, the gas density in these regions is expected to reduce to acceptable values after a few days of continuous operation, perhaps requiring dedicated commissioning runs. If a higher heat load can be accepted then the ESD flux will be correspondingly higher and the conditioning will be quicker. Once the nominal machine parameters are reached the vacuum system is expected to be fully conditioned and performing to specification.

6 Conclusions

It is important in the design of the LHC vacuum system to estimate the dynamic gas density in order to verify that the proposed system meets specification. In this paper the dynamic gas densities in the DSs and the LSS of IR1&5 and IR2&8 are estimated for optics version 6.3. ISD, PSD and ESD determine the dynamic gas density in the LHC. Each are discussed in detail separately and combined to give, for the first time, a global picture of the gas density in these LSS.

Assuming that adequate pumping is installed to ensure vacuum stability ISD in both cryogenic elements (actively cooled beam screens with distributed pumping slots) and room temperature elements (lumped pumping), ISD will not contribute significantly to the dynamic gas density and may therefore be neglected. In order to estimate the contribution from PSD the sources of SR in the DSs and the LSS in IR1&5 and IR2&8 are identified and quantified. Since the PSD and ESD desorption yields change with dose, known as conditioning, certain assumptions have to be made regarding an operation scenario for the machine in the first years. Namely, the beam current is assumed to be <30% of the nominal (0.56A per beam) for 70 days in the first year followed by and increased beam current to 30% of the nominal in the following year. The PSD and ESD yields are discussed in detail using the available data, in particular the conditioning with dose. These inputs are used to estimate the gas densities in the DSs and LSSs in IR1&5 and IR2&8, excluding the experimental beampipes ±20m from the IP, in the first years of operation.

In the first year, the dynamic gas density will be dominated by photon stimulated desorption since BIEM is not anticipated to be significant at this bunch density. The estimated dynamic gas density scales linearly with beam current and is calculated assuming 20% of the nominal. Initially some room temperature regions of the machine may exhibit elevated gas densities, however, they will condition quickly to acceptable levels over the course of the 70 day running period, assuming that the vacuum sectors are not re-exposed to air due to leaks or for reasons of maintenance. The only exception being the TDI where the thermal out-gassing of the proposed graphite for the collimator material, will dominate and remain constant due to it being retracted from the beam after injection and therefore not subject to beam conditioning. Significant improvements to the gas density in the TDI can be made by design, including a judicious choice of material with a low thermal out-gassing rate. The average gas density in the room temperature sectors adjacent to cryogenic elements are dominated by the gas

density at the cold/warm transitions, due to the change in vacuum chamber dimensions thereby intercepting the photon flux and due to the fact that this region is unbaked. Locating pumping as close as physically possible to the cold/warm transition shall limit this local gas density rise and thus ensure an acceptable average gas density over the sector.

In the second year the beam current is assumed to increase to 30% of the nominal with a corresponding increase in photon flux. At and above this current BIEM is expected to become significant and assuming a controllable heat load on the beam screen from the electron cloud, at the level of 200mW/m, ESD is anticipated resulting in an increased gas density. This ESD flux is estimated directly from the deposited power and the calculated electron energy in the cloud. Due to the efficient conditioning of the vacuum chambers with electrons, the gas densities will recover quickly to acceptable levels; the higher the acceptable heat load in the cryogenic elements the more rapid the conditioning will be. It should be noted that the conditions for BIEM depend on the presence of a magnetic field, the vacuum chamber dimensions and the presence of one or two beams in the vacuum chamber. BIEM conditioning is therefore not expected to occur simultaneously around the machine. Dedicated commissioning fills may therefore be required to condition the vacuum chambers before physics runs. Once the nominal machine parameters are reached the vacuum system is expected to be fully conditioned and performing to specification.

These estimated gas densities may be used, for: i) optimisation of the vacuum system layout, ii) estimations of the background to the experiments from proton gas scattering in the IRs and iii) estimations of the hardware activation due to proton losses in the IRs. Care should be taken in using these data since they are based on a specific commissioning scenario and it is assumed that the machine will never be exposed to air due to leaks or accidental venting during maintenance; these assumptions may not be valid in reality. In addition some of the estimations may not be relevant for certain applications, such as the initial gas densities when BIEM become significant, for experimental background simulations since this will be a 'transient state' and will not necessarily be compatible with data taking. Finally it should be noted that these present estimates provide, for the first time, a complete picture of the dynamic gas density in the specific LSS; they deviate from the initial estimates [2] that assumed a purely static vacuum, i.e. considered only thermal out-gassing.

Further theoretical and experimental studies are required to understand better the conditions for BIEM, such as the dependence on chamber dimensions, in the room temperature chambers. Ideally such experimental studies can now be performed with a LHC–like beam in the SPS. In addition such a

beam may be used to closely simulate the performance of the LHC cryogenic vacuum system, particularly during BIEM and in the presence of physisorbed gases accumulated on the inner surface of the beam screen, such as after a magnet quench. BIEM simulations can help identify the critical parameters for the optimisation of the drift vacuum chambers in the IRs, such as dimensions and surface topology.

Annex: Synchrotron radiation in the IRs.

In the arcs and DS the linear photon flux has the highest value of 10^{17} photon/(s·m) at the LHC nominal current I = 0.56A and a critical energy of 44.1 eV. The SR from the last bending magnet (MB) in the DS irradiates some regions of LSS in Ring 1 on the left-hand-side (lhs) and Ring 2 on the right-hand-side (rhs). The photon flux dilution in the LSS (determined previously in reference [3]) between Q7 and D2 as a function of distance from MB shown in Figure 7, assumes a uniform ID 50 mm vacuum chamber. This is an ideal case and in reality may be quite different due to the different vacuum chamber dimensions. Any changes or transitions in a vacuum chamber cross section will either intercept the SR or cast a shadow over the neighbouring vacuum chamber depending whether the transition is decreasing or increasing in dimensions, respectively (see Table 8 below). It should be noted that this estimation differs in the region of D2 from that presented previously [3] due to the assumed geometry of the vacuum chamber in D2.

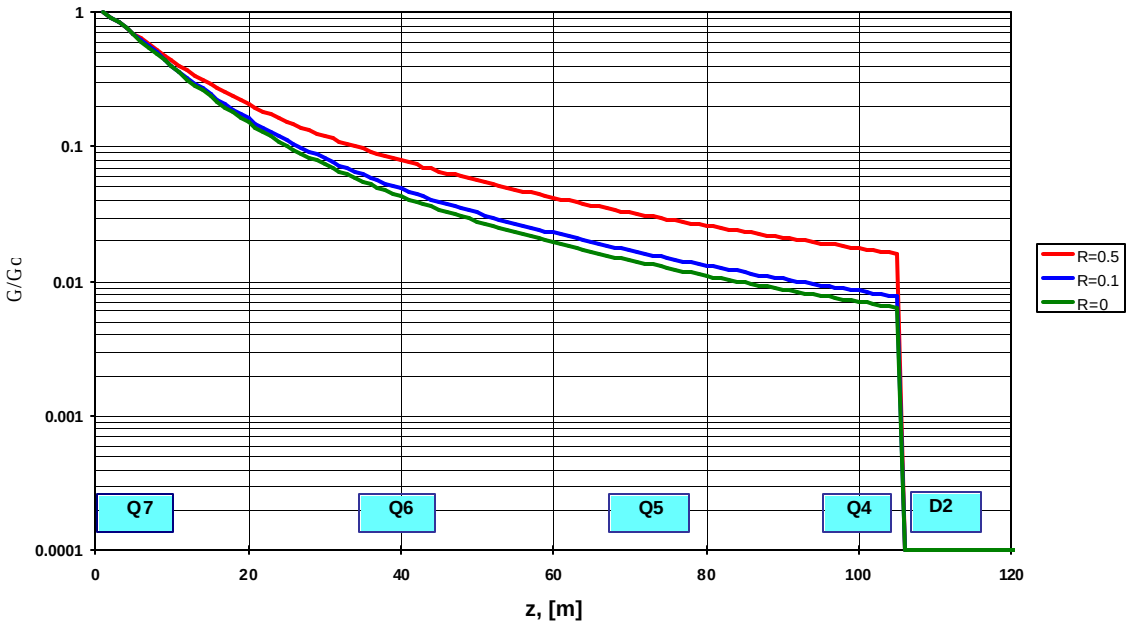

Figure 7. Photon flux from the last MB in the DS as a function of distance along the LSS, for different photon reflectivities. The positions of quadrupoles are shown for LSS1&5.

There exist several other sources of SR in the LSS such as from the quadrupoles and the D1 and D2 dipoles. The SR sources in LSS1&5 and LSS2&8 are presented in Table 4 and Table 6. In these Tables are shown: the angle of irradiation, α, the SR critical energy, e_c, photon flux from the source, $\dot{\Gamma}_s$, and its power, W_s, for one beam. The total photon flux, $\dot{\Gamma}_{tot}$ and total power, W_{tot}, from Inner Triplet, (IT), from the D1 and D2 dipoles, from the Q4–Q7 quadrupoles and from the arc are shown for two beams. These estimations were made previously for optics version 6.1 [29] and do not change significantly for optics version 6.3. The values from the arc dipoles and from the D1 and D2 dipoles are well defined, however, a range of values is given for quadrupoles due the uncertainties in the beam position within the quadrupole. The parameters defining the beam position are the beam off-set used in the crossing scheme (a few mm in IT), the closed orbit deviation (4 mm) and the alignment tolerance of the magnet (1 mm). The estimations are made for the nominal beam current I = 0.56 A and with the photon reflectivity of 65 to 95 % by photon flux or 20 to 50% by SR power.

Table 4. The sources of the synchrotron radiation in LSS1 and LSS5 at nominal beam current. The photon flux G_s and the power W_s are shown for one beam and the total photon flux G_{tot} and power W_{tot} are shown for two beams.

SR source	α, [mrad]	e_c, [eV]	$\dot{\Gamma}_s$, [phot/sec]	W_s, [watt]	$\dot{\Gamma}_{tot}$, [phot/sec]	W_{tot}, [watt]
Q1	0.3–0.8	6–16	$8{\cdot}10^{16}$–$2{\cdot}10^{17}$	0.02–0.17	$9{\cdot}10^{17}$–$1.7{\cdot}10^{18}$	0.4–1.4
Q2	0.3–0.9	6–19	$1.7{\cdot}10^{17}$–$4.5{\cdot}10^{17}$	0.06–0.4		
Q3	0.5–1.0	8–19	$1.2{\cdot}10^{17}$–$2.6{\cdot}10^{17}$	0.05–0.25		
D1	1.1	5.7	$3{\cdot}10^{17}$	0.086	$6{\cdot}10^{17}$	0.17
D2	1.1	14.4	$3{\cdot}10^{17}$	0.217	$6{\cdot}10^{17}$	0.43
Q4	0.1–0.3	2–11	$2{\cdot}10^{16}$–$8{\cdot}10^{16}$	0.002–0.042	$8{\cdot}10^{16}$–$7{\cdot}10^{17}$	0.01–0.28
Q5	0.01–0.3	0.5–7.5	$4{\cdot}10^{15}$–$8{\cdot}10^{16}$	0.0001–0.028		
Q6	0.01–0.3	0.5–7.5	$1{\cdot}10^{15}$–$8{\cdot}10^{16}$	0.0001–0.028		
Q7	0.01–0.5	0.5–8.5	$4{\cdot}10^{15}$–$1.3{\cdot}10^{17}$	0.0001–0.055		
MB	4.2	44.1	$1.15{\cdot}10^{18}$	2.51	$1.15{\cdot}10^{18}$	2.51
Total SR power in LSS1 or LSS5:						7.0–9.6

Table 5. The absorbed SR in the elements of LSS1 and LSS5 at nominal beam current.

	$\dot{\Gamma}_D$, [ph/sec]	P_D, [W]	$\dot{\Gamma}_Q$, [ph/sec]	P_Q, [W]
IT and D1	SR from D1		SR from Q1–Q3	
Q1	$1{\cdot}10^{15}$–$2{\cdot}10^{16}$	0.003–0.007	$< 1{\cdot}10^{18}$	0.2–0.6
Q2	$4{\cdot}10^{15}$–$6{\cdot}10^{16}$	0.01–0.02	$\leq 1{\cdot}10^{18}$	0.2–0.8
Q3	$1{\cdot}10^{15}$–$2{\cdot}10^{16}$	0.004–0.008	$< 1{\cdot}10^{18}$	0.2–0.5
D1	—	—	$1.2{\cdot}10^{17}$–$2.6{\cdot}10^{17}$	0.05–0.25
Total in IT	$< 3{\cdot}10^{17}$	< 0.086	$< 1.5{\cdot}10^{18}$	< 1.3
TAN-conus	$< 2.5{\cdot}10^{17}$	< 0.07	$< 7{\cdot}10^{17}$	< 0.5
Ring 1. The beam from MB to IP				
	SR from MB		SR from Q4–Q7	
TAN	$2{\cdot}10^{16}$–$3{\cdot}10^{16}$	0.01–0.03	$6{\cdot}10^{15}$–$8{\cdot}10^{16}$	0.002–0.03
D2	$5.5{\cdot}10^{16}$–$8{\cdot}10^{16}$	0.026–0.081	$1.5{\cdot}10^{16}$–$2.2{\cdot}10^{17}$	0.005–0.08
Q4	$1.4{\cdot}10^{16}$–$1.8{\cdot}10^{16}$	0.014–0.024	0–$2.0{\cdot}10^{17}$	0–0.08
Q5	$3.0{\cdot}10^{16}$–$3.6{\cdot}10^{16}$	0.032–0.052	0–$1.3{\cdot}10^{17}$	0–0.05
Q6	$7.2{\cdot}10^{16}$–$7.7{\cdot}10^{16}$	0.093–0.134	—	—
VC	$4.0{\cdot}10^{17}$–$4.7{\cdot}10^{17}$	0.79–0.96	—	—
Q7	$6.0{\cdot}10^{17}$–$6.3{\cdot}10^{17}$	1.33–1.37	—	—
Total D2–Q7	$1.15{\cdot}10^{18}$	2.51	$3.7{\cdot}10^{16}$–$3.5{\cdot}10^{17}$	0.005–0.14
Ring 2. The beam from IP to MB				
	SR from D2		SR from Q4–Q7	
TAN, D2, Q4	—	—	—	—
Q5	$3.0{\cdot}10^{16}$	0.021	—	—
Q6	$1.0{\cdot}10^{16}$	0.007	0–$6{\cdot}10^{16}$	0–0.03
VC	$2.0{\cdot}10^{16}$	0.015	0–$1.4{\cdot}10^{17}$	0–0.06
Q7	$6.0{\cdot}10^{15}$	0.004	0–$1.4{\cdot}10^{17}$	0–0.06
Total D2–Q7	$3{\cdot}10^{17}$	0.3	$4{\cdot}10^{16}$–$1.6{\cdot}10^{17}$	0.01–0.07

Table 6. The sources of the synchrotron radiation in LSS2 and LSS8 at nominal beam current. The photon flux Γ_s and the power W_s are shown for one beam and the total photon flux Γ_{tot} and power W_{tot} are shown for two beams.

SR from	α, [mrad]	e_c, [eV]	$\dot{\Gamma}_s$, [phot/sec]	W_s, [watt]	$\dot{\Gamma}_{tot}$, [phot/sec]	W_{tot}, [watt]
Q1	0.3–0.8	6–16	$8{\cdot}10^{16}$–$2{\cdot}10^{17}$	0.02–0.17	$9{\cdot}10^{17}$–$1.7{\cdot}10^{18}$	0.4–1.4
Q2	0.3–0.9	6–19	$1.7{\cdot}10^{17}$–$4.5{\cdot}10^{17}$	0.06–0.4		
Q3	0.5–1.0	8–19	$1.2{\cdot}10^{17}$–$2.6{\cdot}10^{17}$	0.05–0.25		
D1	1.52	19.7	$4.1{\cdot}10^{17}$	0.403	$8.2{\cdot}10^{17}$	0.81
D2	1.52	19.7	$4.1{\cdot}10^{17}$	0.403	$8.2{\cdot}10^{17}$	0.81
Q4	0.1–0.3	2–11	$2{\cdot}10^{16}$–$8{\cdot}10^{16}$	0.002–0.042	$8{\cdot}10^{16}$–$7{\cdot}10^{17}$	0.01–0.28
Q5	0.01–0.3	0.5–7.5	$4{\cdot}10^{15}$–$8{\cdot}10^{16}$	0.0001–0.028		
Q6	0.01–0.3	0.5–7.5	$1{\cdot}10^{15}$–$8{\cdot}10^{16}$	0.0001–0.028		
Q7	0.01–0.5	0.5–8.5	$4{\cdot}10^{15}$–$1.3{\cdot}10^{17}$	0.0001–0.055		
MB	4.2	44.1	$1.15{\cdot}10^{18}$	2.51	$1.15{\cdot}10^{18}$	2.51
Total SR power in LSS2 or LSS8:						9.4–11.8

Table 7. The absorbed SR in the elements of LSS2 and LSS8 at nominal beam current.

Magnet	$\dot{\Gamma}_D$, [ph/sec]	P_D, [W]	$\dot{\Gamma}_Q$, [ph/sec]	P_Q, [W]
IT	SR from D1		SR from Q1–Q3	
Q1	$2{\cdot}10^{15}$–$3{\cdot}10^{16}$	0.01–0.02	$< 1{\cdot}10^{18}$	0.2–0.6
Q2	$6{\cdot}10^{15}$–$9{\cdot}10^{16}$	0.04–0.08	$\leq 1{\cdot}10^{18}$	0.2–0.8
Q3	$3{\cdot}10^{15}$–$5{\cdot}10^{16}$	0.02–0.04	$< 1{\cdot}10^{18}$	0.2–0.5
D1	—	—	$1.2{\cdot}10^{17}$–$2.6{\cdot}10^{17}$	0.05–0.25
Total in IT	$< 4{\cdot}10^{17}$	< 0.3	$< 1.5{\cdot}10^{18}$	< 1.3
Ring 1. The beam from MB to IP				
	SR from MB		SR from Q4–Q7	
D2	$8.3{\cdot}10^{16}$–$1.3{\cdot}10^{17}$	0.037–0.12	$1.0{\cdot}10^{16}$–$2.0{\cdot}10^{17}$	0.004–0.08
Q4	$1.6{\cdot}10^{16}$–$2.2{\cdot}10^{16}$	0.015–0.027	0–$2.0{\cdot}10^{17}$	0–0.08
Q5	$2.7{\cdot}10^{16}$–$3.4{\cdot}10^{16}$	0.026–0.045	0–$1.3{\cdot}10^{17}$	0–0.06
Q6	$1.4{\cdot}10^{17}$–$1.5{\cdot}10^{17}$	0.22–0.29	—	—
DFBA	$2.0{\cdot}10^{17}$–$3.0{\cdot}10^{17}$	0.54–0.63	—	—
Q7	$6.0{\cdot}10^{17}$–$6.3{\cdot}10^{17}$	1.33–1.37	—	—
Total D2–Q7	$1.15{\cdot}10^{18}$	2.51	$3.7{\cdot}10^{16}$–$3.5{\cdot}10^{17}$	0.005–0.14
Ring 2. The beam from IP to MB				
	SR from D2		SR from Q4–Q7	
D2, Q4	—	—	—	—
Q5	$3.1{\cdot}10^{16}$	0.069	—	—
Q6	$5.0{\cdot}10^{15}$	0.011	0–$8{\cdot}10^{16}$	0–0.03
DFBA	$4.7{\cdot}10^{15}$	0.01	0–$1.6{\cdot}10^{17}$	0–0.06
Q7	$3.5{\cdot}10^{15}$	0.007	0–$1.6{\cdot}10^{17}$	0–0.06
Total D2–Q7	$4.1{\cdot}10^{17}$	0.4	$4{\cdot}10^{16}$–$1.6{\cdot}10^{17}$	0.01–0.07

Table 8. The shadow and photon flux at each cold-warm transition (CWT).

Vacuum chamber Location	Length (m)	Shadowed	Photon flux at CWT	
			Location of CWT	Photons/s at nominal current
LSS1&5				
Ring 1. The beam from MB to IP, SR from MB and Q4–Q7.				
TAN to D2 D2	7.5 11.67	Fully Fully	— —	— —
Q4 to Q5	19.38	Fully	Q4	$7 \cdot 10^{16}$
Q5 to Q6	24.76	18.5 m from Q6	Q5	$1.3 \cdot 10^{17}$
Q6 to DFBA	17.73	7.5 m from DFBA	Q6	$2.5 \cdot 10^{17}$
Ring 2. The beam from IP to MB, SR from D1, D2 and Q4–Q7.				
TAN to D2	7.5	Fully	—	—
D2+Q4	20.32	Fully	—	—
Q4 to Q5	19.38	Fully	Q5	$2 \cdot 10^{17}$
Q5 to Q6	24.76	16 m from Q5	Q6	$1.5 \cdot 10^{17}$
Q6 to DFBA	17.73	Fully	Q7	$8 \cdot 10^{16}$
LSS2&8				
Ring 1. The beam from MB to IP, SR from MB and Q4–Q7.				
X2ZDC to D2	2.76	Fully	—	—
D2	11.41	Fully	—	—
Q4 to Q5	16.74	Fully	Q4	$5 \cdot 10^{16}$
Q5 to Q6	60.96	14.5 m from Q6	Q5 (ID42.4) Q5 (ID56.4)	$1 \cdot 10^{17}$ $7 \cdot 10^{16}$
Q6 to Q7	14.78	2.0 m from Q7	Q6	$1.3 \cdot 10^{17}$
Ring 2. The beam from IP to MB, SR from D1, D2 and Q4–Q7.				
X2ZDC to D2	2.76	Fully	—	—
D2+Q4	24.14	Fully	—	—
Q4 to Q5	16.74	Fully	Q5 (ID42.4) Q5 (ID56.4)	$3 \cdot 10^{17}$ $2 \cdot 10^{17}$
Q5 to Q6	60.96	20 m from Q5 (ID42.4) 13 m from Q5 (ID56.4)	Q6	$9 \cdot 10^{16}$
Q6 to Q7	14.78	Fully	Q7	$2 \cdot 10^{16}$

As one can see from Table 4 and Table 6 the SR from the dipoles and quadrupoles in the LSS can be significant in most cases with fluxes comparable to those in the arc, however distributed over a longer distance. These fluxes should therefore be taken into account in estimations of the gas density in the LHC.

It is also important to estimate where the SR will be adsorbed. The SR fluxes and powers adsorbed on all cryogenic elements are shown in Table 5 and Table 7, respectively from the dipoles

with subscript D and from the quadrupoles with subscript Q. SR from the arcs in the LSS has less intensity, as shown in Figure 7, with the same critical energy ~44.1 eV [3]. D1, D2 and the quadrupoles produce SR with a lower intensity and a lower critical energy than that in the arc. The photodesorption flux per unit length of LSS is therefore less or equal to that in the arcs. As previously mentioned any transition or change in a vacuum chamber cross-section, such as at a CWT, will either intercept the SR or cast a shadow over the neighbouring chamber. The length of shadowed vacuum chambers after transitions, location and photon flux intensities of adsorbed photons are shown in Table 8. It is therefore recommended as a good design principle to incorporate lumped pumping, as close as physically possible, to these locations that represent a significant source of gas.

References:

[1] P.Cruikshank *et al.* "General parameters for equipment installed in the LHC." LHC-PM-ES-0002

[2] A. G. Mathewson. "First estimates of the gas density in the LHC. Workshop on LHC backgrounds." 22nd March 1996. CERN.

[3] O.B. Malyshev and I.R. Collins. "Estimates of photon induced gas densities in the Long Straight Sections of IR1 and IR5 for v6.0 of the LHC." Vacuum Technical Note 99-14, November 1999, CERN. http://wwwlhc.cern .ch/VAC/VACPAGES/VacuumTechNote/1999/TN_99_14.pdf

[4] V.V. Anashin, O.B. Malyshev, V.N. Osipov, I.L. Maslennikov and W.C. Turner. "Investigation of synchrotron radiation-induced photodesorption in cryosorbing quasi-closed geometry", J.Vac.Sci.Technol. A 12(5), pp. 2917–2921, Sep/Oct 1994.

[5] W. Turner. "Beam tube vacuum in future superconducting proton colliders", SSCL-Preprint-564, Oct 1994.

[6] O. B. Malyshev and A. Rossi. "Ion desorption stability in the LHC." Vacuum Technical Note 99-20, December 1999, CERN. - 76 p. http://wwwlhc.cern.ch/VAC/VACPAGES/VacuumTechNote/1999/TN_99_20.pdf

[7] J. Gómez-Goñi, O. Gröbner and A.G. Mathewson. "Exposure of an OFHC Cu-lined chamber to photons." Vacuum Technical Note 92-06, CERN, July 1992.

[8] J. Gómez-Goñi, O. Gröbner and A.G. Mathewson. "Continued exposure of an OFHC Cu-lined chamber to photons." Vacuum Technical Note 92-12, CERN, October 1992.

[9] I. Maslennikov, W. Turner, *et al*. "Photon desorption measurements of copper and copper plated beam tubes for the SSCL 20 TeV proton collider." J.Vac.Sci.Technol A12(4), Jul/Aug 1994, pp.1673–1677.

[10] R. Calder, O. Gröbner, A.G. Mathewson, V.V. Anashin, A. Dranichnikov, O. Malyshev. "Synchrotron radiation induced gas desorption from a prototype Large Hadron Collider beam screen at cryogenic temperatures." J. Vac. Sci. Technol. A 14(4), pp. 2618–2623, Jul/Aug 1996. (CERN AT/95-42 (VA). LHC Project Note 7). http://preprints.cern.ch/archive/electronic/cern/others/LHC/Note/project-note-7.pdf

[11] O.B. Malyshev. Thesis: 'The study of photodesorption processes in the prototypes of vacuum chamber of Superconducting Super Colliders." BINP, Novosibirsk, 1995.

[12] O. Bruning. "Simulation for the beam induced electron cloud in the LHC liner." LHC Project Note 102, 1997.

[13] M.Furman. "The electron cloud effect for LHC." Proceedings of the International workshop on multibunch instabilites in future electron and positron colliders, Tsukuba, Japan, 1997.

[14] S.Berg. "Energy gain in an electron cloud during the passage of a bunch." LHC Project Note 97.

[15] J. Gómez-Goñi. "Temperature dependence of the electron induced gas desorption yields from 316LN stainless steel, OFHC and Al samples." Vacuum Technical Note 94-16, CERN, July 1994.

[16] O.Bruning *et al.* "Electron cloud and beam scrubbing in the LHC." LHC Project Report 290

[17] J. Gómez-Goñi and A.G. Mathewson. "Temperature dependence of the electron induced gas desorption yields on stainless steel, copper and aluminum." J. Vac. Sci. Technol. A 15(6), pp. 3093–3103, Nov/Dec 1997.

[18] F. Billard, N. Hilleret and G. Vorlaufer. "Some results on the electron induced desorption yield of OFHC copper." Vacuum Technical Note 00-32, December 2000.

[19] K. Kennedy. "Electron stimulated desorption rates from candidate vacuum chamber surfaces." LBL, Berkeley, July 1986.
[20] M.H. Achard, R. Calder and A. Mathewson. "The effect of bakeout temperature on the electron and ion induced gas desorption coefficients of some technological materials." Vacuum, v.29(2), pp. 53–59, 1978.
[21] L.Evans. Private communication.
[22] F. Zimmerman. "Electron cloud simulations for SPS and LHC." Proceedings of Chamonix X, CERN-SL-2000-007-DI
[23] O.B. Malyshev. "The capture factor and pumping speed for slots in the LHC beam screen." Vacuum Technical Note 00-17, August 2000, CERN. - 20 p.
http://wwwlhc.cern.ch/VAC/VACPAGES/VacuumTechNote/2000/TN_00_17.pdf
[24] A.Rossi Private communication
[25] O. Gröbner. "The LHC vacuum system." LHC Project Report 181.
http://preprints.cern.ch/archive/electronic/cern/preprints/lhc/lhc-project-report-181.pdf
[26] F.Zimmermann. "Electron-cloud simulations for the LHC straight sections." LHC Project Report 201.
[27] M. Jimenez. Private communication
[28] "ALICE Technical design report of the zero degree calorimeter." CERN LHCC 99-05. ALICE TDR 3 (March 1999).
[29] Presented at the 24th IRWG on 27th May 1999. See minutes:
http://hprin.home.cern.ch/hprin/minutes/irwg_24.pdf